

# Phase diagrams of binary ionic mixtures and white dwarf cooling

D. A. Baiko<sup>\*</sup>

*A. F. Ioffe Physical-Technical Institute, Politekhnikeskaya 26, 194021 St.-Petersburg, Russia*

Accepted; Received ; in original form

## ABSTRACT

Phase diagrams of fully ionized binary ionic mixtures are considered within the framework of the linear mixing formalism taking into account recent advances in understanding quantum one-component plasma thermodynamics. We have followed a transformation of azeotropic phase diagrams into peritectic and eutectic types with increase of the charge ratio. For solid  $^{12}\text{C}/^{16}\text{O}$  and  $^{16}\text{O}/^{20}\text{Ne}$  mixtures, we have found extensive miscibility gaps. Their appearance seems to be a robust feature of the theory. The gaps evolve naturally into two-solid regions of eutectic phase diagrams at higher  $Z_2/Z_1$ . They do not depend on thermodynamic fit extensions beyond their applicability limits. The gaps are sensitive to binary mixture composition and physics, being strongly different for C/O and O/Ne mixtures and for the three variants of corrections to linear-mixing solid-state energies available in the literature. When matter cools to its miscibility gap temperature, the exsolution process takes place. It results in a separation of heavier and lighter solid solutions. This may represent a significant reservoir of gravitational energy and should be included in future white dwarf (WD) cooling simulations. Ion quantum effects mostly resulted in moderate modifications, however, for certain  $Z_2/Z_1$ , these effects can produce qualitative restructuring of the phase diagram. This may be important for the model with  $^{22}\text{Ne}$  distillation in cooling C/O/Ne WD proposed as a solution for the ultramassive WD cooling anomaly.

**Key words:** dense matter – equation of state – white dwarfs – stars: neutron.

## 1 INTRODUCTION

A good model of matter for such astrophysical objects as interior layers of white dwarfs (WD) and outer neutron star crust is a fully ionized binary ionic mixture (BIM). This is a system of point charges (ions) of two sorts, with different charge and/or mass numbers, immersed into a degenerate nearly incompressible electron gas. Under realistic conditions, depending on matter density and temperature, BIM can be in a liquid or crystallized state.

Various BIM properties are important for astrophysical applications. Since liquid and solidified BIM at equilibrium with each other, typically, must have different fractions of constituents, ion crystallization in a BIM is accompanied by separation of ion species. This leads to gravitational energy release. Combined with latent heat release, this effect appears to be crucial for WD cooling theory. Recent *Gaia* observations (Gaia Collaboration et al. 2018) indicate a pile-up of WD on the so-called Q branch, which implies significant additional cooling delay likely associated with other aspects of crystallization physics (e.g. Tremblay et al.

2019; Cheng, Cummings & Ménard 2019; Bauer et al. 2020; Caplan, Horowitz & Cumming 2020; Camisassa et al. 2021; Blouin, Daligault & Saumon 2021).

Ion structure factor and degree of disorder have an impact on electron thermal and electric conduction (e.g. Flowers & Itoh 1976; Yakovlev & Urpin 1980; Daligault & Gupta 2009; Roggero & Reddy 2016; Caplan 2020; Fantina et al. 2020), which, in turn, determine thermal profile of compact stars and evolution of their magnetic fields. Ion correlations and screening modify thermonuclear reaction rates by many orders of magnitude and even allow pycnonuclear burning at zero temperature (e.g. Yakovlev & Shalybkov 1989; Ichimaru 1993). This affects composition of accreted crust in low-mass X-ray binaries (e.g. Lau et al. 2018; Shchepochin & Chugunov 2019) as well as regimes and outcomes of helium burning in accreting WD (e.g. Piersanti, Tornambé & Yungelson 2014).

Thermodynamics of BIM has been the subject of intensive research (e.g. Segretain & Chabrier 1993; Ogata et al. 1993; DeWitt & Slattery 2003; Medin & Cumming 2010; Horowitz et al. 2010; Blouin et al. 2020). Due to strong coupling, first-principle simulations are preferred to obtain reliable information on the properties of the system. Moreover,

<sup>\*</sup> E-mail: baiko@astro.ioffe.ru

there is an important corner of the parameter space, where relatively light ions (e.g. helium or carbon) occur at fairly high densities, so that ion quantum effects are already pronounced but pycnonuclear fusion is not yet rapid enough. In this regime, first-principle *quantum* simulations are desirable.

Another approach is based on the idea that BIM thermodynamics can be recovered with reasonable accuracy via “linear mixing” from thermodynamics of appropriate single-species ion systems (known as one-component plasmas or OCP). This is certainly less expensive than first-principle simulations of BIM. However, besides OCP thermodynamics, this approach relies on the knowledge of “corrections” to linear-mixing quantities to make the results more realistic. Also, it inevitably requires usage of OCP thermodynamic fits at temperatures far beyond the aggregate states, for which they have been designed, or replacement of the fits by extrapolations (e.g. Medin & Cumming 2010; Jermyn et al. 2021).

In this work, we focus on phase transition properties of BIM within this linear mixing with corrections framework. We aim to take advantage of the fact that quantum OCP thermodynamics has been recently developed both in the liquid and in the solid phases (Baiko 2019; Baiko & Yakovlev 2019; Baiko & Chugunov 2022). In particular, in the solid phase, in addition to the well-known quantum harmonic thermodynamics (e.g. Baiko, Potekhin & Yakovlev 2001), quantum anharmonic functions have been calculated and parameterized. This allows one, for the first time, to include ion quantum effects into BIM phase diagram construction. All previous calculations of this sort were strictly classic.

The paper is organized as follows. In sections 2 and 3, we reproduce the standard expressions for BIM free energies in the liquid and solid phases, respectively, paying special attention to still existing theoretical uncertainties. In section 4, we formulate equilibrium equations, which determine melting/crystallization and solid solubility curves on a phase diagram. Phase diagrams for C/O and O/Ne mixtures are analyzed in detail in sections 5.1 and 5.2, respectively. Astrophysical implications of miscibility gaps discovered in C/O and O/Ne systems are discussed in section 5.3. In section 5.4, we follow a sequence of phase diagrams for systems with intermediate charge ratios (including O/Mg, C/Ne, O/Si, and C/Mg mixtures), which illustrates a diagram transformation from azeotropic to peritectic and finally to eutectic type. Phase diagrams for C/Ne and C/Mg mixtures are considered in more detail in section 5.5, where we also make a few remarks on  $^{22}\text{Ne}$  distillation process in cooling C/O/Ne WD (Blouin et al. 2021) and on eutectic system cooling. Section 5.6 is devoted to the phase diagram of a He/C mixture. We conclude in section 6.

## 2 FREE ENERGY OF THE LIQUID PHASE

The Helmholtz free energy of an OCP,  $F_{\text{OCP}}$ , can be written as

$$F_{\text{OCP}}(N, V, T, Z, m) \equiv NT f_{\text{OCP}}(N/V, T, Z, m), \quad (1)$$

where  $N$  is the number of ions,  $V$  is the volume,  $T$  is the temperature,  $Z$  is the ion charge number, and  $m$  is the ion mass. In this way, the reduced Helmholtz free energy  $f$  (per

particle, measured in units of  $T$ ) is conveniently introduced ( $k_B \equiv 1$ ). The same definition will be adopted also for various partial contributions to the free energy.

In a liquid phase (‘*liq*’), it is customary and convenient to separate the standard ideal gas contribution (‘*id*’) and a correction due to the system non-ideality (i.e. having to do with Coulomb interactions: ‘*nid*’):

$$\begin{aligned} F_{\text{OCP}}^{\text{liq}} &\equiv NT f_{\text{OCP}}^{\text{liq}} \\ &= F_{\text{id}} + F_{\text{nid}} \equiv NT[f_{\text{id}}(\Gamma, \theta) + f_{\text{nid}}(\Gamma, \theta)]. \end{aligned} \quad (2)$$

It is well-known, that the reduced free energy in the OCP model depends on just two dimensionless combinations of physical parameters:  $\Gamma = \Gamma(n, T, Z) = Z^2 e^2 / (aT)$  and  $\theta = \theta(n, T, Z, m) = T_p / T$ . In this case,  $a = (4\pi n/3)^{-1/3}$  is the ion Wigner-Seitz radius,  $n = N/V$  is the ion number density, and  $T_p = \hbar \sqrt{4\pi n Z^2 e^2 / m}$  is the ion plasma temperature.

Furthermore, the non-ideal contribution can be split into classic (‘*cl*’) and quantum (‘*q*’) terms:

$$F_{\text{nid}} = F_{\text{nid cl}} + F_{\text{nid q}} \equiv NT[f_{\text{nid cl}}(\Gamma) + f_{\text{nid q}}(\Gamma, \theta)], \quad (3)$$

and the classic term,  $f_{\text{nid cl}}$ , is known to be a function of just one parameter,  $\Gamma$ .

Suppose we have a BIM of  $N_1$  and  $N_2$  ions characterized by charge numbers  $Z_1$  and  $Z_2$  and masses  $m_1$  and  $m_2$ , respectively. Throughout the paper, we shall assume that  $Z_2 > Z_1$ . We want to come up with a reasonable approximation for thermodynamic functions of this BIM based on detailed knowledge of the OCP thermodynamics. The electron number density in the mixture is  $n_e = (Z_1 N_1 + Z_2 N_2) / V$ . Then, in spite of the fact that the actual density of the  $j$ th type ions in the mixture is  $N_j / V$ ,  $j = 1, 2$ , one is physically motivated to employ non-ideal quantities of the  $j$ th type OCP at ion density  $n_e / Z_j$ , which would imply the same electron density in the OCP as in the BIM. By contrast, the ideal quantities must depend on true ion number densities.

Thus, according to the standard linear mixing (‘LM’) prescription, for a classic liquid,

$$\begin{aligned} \frac{F_{\text{BIM cl}}^{\text{liq}}}{T} &= \frac{F_{12 \text{id}}}{T} + N_1 f_{1 \text{nid cl}} + N_2 f_{2 \text{nid cl}} \\ &+ (N_1 + N_2) \Delta f_{\text{nLM}}^{\text{liq}}. \end{aligned} \quad (4)$$

In this case,  $F_{12 \text{id}}(N_1, N_2, V, T, m_1, m_2)$  is the free energy of a mixture of two ideal gases with densities  $N_1/V$  and  $N_2/V$ ,  $f_{j \text{nid cl}} = f_{\text{nid cl}}(\Gamma_j)$ ,

$$\Gamma_j = \Gamma\left(\frac{n_e}{Z_j}, T, Z_j\right) = \frac{Z_j^{5/3} e^2}{a_e T}, \quad (5)$$

and  $a_e = (4\pi n_e/3)^{-1/3}$ . Finally,  $\Delta f_{\text{nLM}}^{\text{liq}}$  is a correction to the linear mixing rule in the liquid (‘nLM’ for ‘non-linear-mixing’), which can be obtained from a first-principle simulation of the mixture or from a more advanced theory.

Let us note, that the use of  $F_{12 \text{id}}$  in equation (4) ensures that, in the limit of high temperatures, the entropy of the mixture contains, as it should, mixing entropy of two ideal gases with  $N_1$  and  $N_2$  particles (e.g. Landau & Lifshitz 1980):

$$S_{\text{mix}} = N_1 \ln \frac{N_1 + N_2}{N_1} + N_2 \ln \frac{N_1 + N_2}{N_2}. \quad (6)$$

For a quantum liquid, the prescription (4) can be ex-

tended in the natural way:

$$\frac{F_{\text{BIM}}^{\text{liq}}}{T} = \frac{F_{12\text{id}}}{T} + N_1 f_{1\text{id}} + N_2 f_{2\text{id}} + (N_1 + N_2) \Delta f_{\text{nLM}}^{\text{liq}}, \quad (7)$$

where  $f_{j\text{id}} = f_{\text{id}}(\Gamma_j, \theta_j)$ , and

$$\theta_j = \theta \left( \frac{n_e}{Z_j}, T, Z_j, m_j \right) = \frac{\hbar}{T} \sqrt{\frac{4\pi n_e Z_j e^2}{m_j}}. \quad (8)$$

Equation (7) can be rewritten identically as

$$\begin{aligned} \frac{F_{\text{BIM}}^{\text{liq}}}{T} &= N_1 f_{1\text{OCP}}^{\text{liq}} + N_2 f_{2\text{OCP}}^{\text{liq}} - S_{\text{mixZ}} \\ &+ (N_1 + N_2) \Delta f_{\text{nLM}}^{\text{liq}}, \end{aligned} \quad (9)$$

where  $f_{j\text{OCP}}^{\text{liq}} = f_{\text{id}}(\Gamma_j, \theta_j) + f_{\text{id}}(\Gamma_j, \theta_j)$ , and

$$S_{\text{mixZ}} = N_1 \ln \frac{Z_1 N_1 + Z_2 N_2}{Z_1 N_1} + N_2 \ln \frac{Z_1 N_1 + Z_2 N_2}{Z_2 N_2}. \quad (10)$$

In practical calculations, we shall take the quantity  $f_{\text{id}}$  as a sum of classic fit of Potekhin & Chabrier (2000) and quantum fit of Baiko & Chugunov (2022) at all required temperatures. Unfortunately, no information on quantum corrections to the linear mixing is presently available, thus, we can only use the same  $\Delta f_{\text{nLM}}^{\text{liq}}$  from classic equation (4) in quantum equations (7) and (9). In what follows, we shall utilize the fitting formula for  $\Delta f_{\text{nLM}}^{\text{liq}}$  from Potekhin et al. (2009) and shall include this quantity in all our calculations.

### 3 FREE ENERGY OF THE SOLID PHASE

In a solid phase ('sol'), the reduced free energy of the OCP reads

$$f_{\text{OCP}}^{\text{sol}} = f_{\text{Mad}}(\Gamma) + f_{\text{h}}(\theta) + f_{\text{ah}}(\Gamma, \theta), \quad (11)$$

where indices 'Mad', 'h', and 'ah' stand for Madelung, harmonic, and anharmonic contributions, respectively.

In the linear mixing formalism, in analogy with equation (9), the Helmholtz free energy of a binary solid mixture is written as

$$\begin{aligned} \frac{F_{\text{BIM}}^{\text{sol}}}{T} &= N_1 f_{1\text{OCP}}^{\text{sol}} + N_2 f_{2\text{OCP}}^{\text{sol}} - S_{\text{mixZ}} \\ &+ (N_1 + N_2) \Delta f_{\text{nLM}}^{\text{sol}}. \end{aligned} \quad (12)$$

This can be rewritten identically as

$$\begin{aligned} \frac{F_{\text{BIM}}^{\text{sol}}}{T} &= \frac{F_{12\text{id}}}{T} + N_1 (f_{1\text{OCP}}^{\text{sol}} - f_{1\text{id}}) + N_2 (f_{2\text{OCP}}^{\text{sol}} - f_{2\text{id}}) \\ &+ (N_1 + N_2) \Delta f_{\text{nLM}}^{\text{sol}}. \end{aligned} \quad (13)$$

In this case,  $f_{j\text{id}} = f_{\text{id}}(\Gamma_j, \theta_j)$ , while  $\Delta f_{\text{nLM}}^{\text{sol}}$  is a correction to the linear mixing prescription in the solid phase, which must be deduced from more advanced studies. Let us emphasize once again, that  $F_{12\text{id}}$  employs actual ion number densities, whereas  $f_{j\text{id}}$  is calculated for the "effective"  $j$ th ion density equal to  $n_e/Z_j$ . In practical calculations,  $f_{j\text{OCP}}^{\text{sol}} = f_{\text{OCP}}^{\text{sol}}(n_e/Z_j, T)$  will be given by a sum of the Madelung energy, harmonic quantum fit of Baiko et al. (2001), and anharmonic quantum fit of Baiko & Chugunov (2022) at all required temperatures (but see Fig. 7a and section 5.6).

Presently, there exist three different parameterizations of  $\Delta f_{\text{nLM}}^{\text{sol}}$ . Two of them (Ogata et al. 1993;

DeWitt & Slattery 2003) are based on first-principle classic simulations of solid mixtures. In reality, they include only a correction to the Madelung energy. The third one (Potekhin & Chabrier 2013) is an interpolation, attempting to extend the results of DeWitt & Slattery (2003) to higher charge number ratios.

In Fig. 1a, we compare these parameterizations as functions of the heavier element fraction,  $x_2 = N_2/(N_1 + N_2)$ , for several  $Z_2/Z_1$  marked near the curves. Thick (red), thin (blue), and intermediate (green) curves represent parameterizations of Ogata et al. (1993), DeWitt & Slattery (2003), and Potekhin & Chabrier (2013), respectively. Vertical axis shows  $\Delta f$  in units of  $\Gamma_1 \equiv Z_1^{5/3} \Gamma_e$  (such normalization is marked by a tilde). It is noteworthy, that, for C/O mixture, parameterizations of DeWitt & Slattery (2003) and Potekhin & Chabrier (2013) predict noticeably larger  $\Delta f_{\text{nLM}}^{\text{sol}}$  than does the parameterization of Ogata et al. (1993) in a wide range of  $x_2$ . Another significant difference is seen in the behaviour of the parameterizations at low  $x_2$ .

Let us observe, that equation (12) seems somewhat artificial, because, in the solid phase, in view of the melting phase transition, there is no requirement to reproduce the correct mixing entropy of ideal gases at high temperatures. On the other hand, at low temperatures, the prescription (12) or (13) results in the residual entropy of the solid mixture at  $T = 0$  equal to  $S_{\text{mixZ}}$  ( $f_{\text{OCP}}^{\text{sol}}$  yields zero entropy at  $T = 0$ ), justification for which is not clear. For instance, the entropy of a random alloy, with ions of two types occupying randomly nodes of a perfect crystal lattice, is given by

$$\begin{aligned} \ln \frac{(N_1 + N_2)!}{N_1! N_2!} &\approx S_{\text{mix}} \\ &= N_1 \ln \frac{N_1 + N_2}{N_1} + N_2 \ln \frac{N_1 + N_2}{N_2}. \end{aligned} \quad (14)$$

Thus, one is tempted to try an alternative expression for  $F_{\text{BIM}}^{\text{sol}}$ , which is obtained from equation (12) by replacement  $S_{\text{mixZ}} \rightarrow S_{\text{mix}}$ . In what follows, we shall analyze phase diagram changes stemming from such a replacement.

### 4 EQUILIBRIUM CONDITIONS

In order to construct a phase diagram, one has to determine physical conditions, at which different phases are in thermodynamic equilibrium. In view of a very high electron thermal conductivity, we assume that the phases are at a fixed temperature  $T$ . The phases must be also at the same pressure. However, the pressure is not convenient to work with, because thermodynamic functions, such as the energy or the Helmholtz free energy, are calculated microscopically at given particle densities.

The pressure is dominated by the contribution of degenerate electrons. Hence, the easiest approach is to assume that the electron density  $n_e$  is the same in all phases. This approach neglects the fact that, in reality, there is a jump of electron density and pressure at phase boundaries (compensated by an ion pressure jump, cf. Baiko & Chugunov 2022), which affects the Helmholtz free energies and ion chemical potentials derived from them. A more self-consistent approach would be to switch to Gibbs free energies. This has been done, e.g., by Medin & Cumming (2010) within the framework of the perturbation theory. There was a differ-

ence between results obtained by the two approaches but it has not been found to be drastic. Blouin & Daligault (2021) also independently showed (using first-principle simulations) that volume changes during the phase transition can be neglected.

In the present paper, we adopt an intermediate approach, where we take into account the electron pressure jump only in the leading terms of the Helmholtz free energy.

The chemical potentials of ion species 1 and 2 can be found in the liquid and solid phases as

$$\mu_{1,2}^{\ell iq, sol} = \left( \frac{\partial F_{BIM}^{\ell iq, sol}}{\partial N_{1,2}} \right)_{N_{2,1}, V, T} . \quad (15)$$

If there is an equilibrium, the chemical potentials of both ion species in the liquid and solid phases must be equal:

$$\mu_1^{\ell iq} = \mu_1^{sol} , \quad (16)$$

$$\mu_2^{\ell iq} = \mu_2^{sol} . \quad (17)$$

These equations form the basis of the phase diagram construction.

In addition to the ion contributions to the Helmholtz free energy, there is also an electron contribution, which can be approximated by the energy of the zero-temperature electron gas:

$$F_{BIM} \rightarrow F_{BIM} + E_e = F_{BIM} + \frac{V}{\pi^2} \int_0^{k_F(n_e)} dk k^2 \varepsilon_k ,$$

where  $k_F(n_e) = (3\pi^2 n_e)^{1/3}$  is the electron Fermi wavevector, and  $\varepsilon_k$  is the electron energy at wavevector  $k$ . Such a correction to  $F_{BIM}$  results in a modification of the ion chemical potentials:

$$\begin{aligned} \mu_{1,2}^{\ell iq, sol} &\rightarrow \mu_{1,2}^{\ell iq, sol} + \Delta \mu_{1,2}^{\ell iq, sol} \\ &\equiv \mu_{1,2}^{\ell iq, sol} + Z_{1,2} \varepsilon_{k_F}(n_e^{\ell iq, sol}) , \end{aligned} \quad (18)$$

where  $\varepsilon_{k_F}$  is the electron Fermi energy, and we have stressed its dependence on  $n_e$ .

Making such an adjustment to the chemical potentials in equations (16) and (17) (divided by  $Z_1$  and  $Z_2$ , respectively), and subtracting the second of them from the first one, we obtain an equilibrium condition in the form

$$\frac{\mu_1^{\ell iq} - \mu_1^{sol}}{Z_1} - \frac{\mu_2^{\ell iq} - \mu_2^{sol}}{Z_2} = 0 . \quad (19)$$

In this way, the electron Fermi energy, which is large and slightly different in the liquid and solid phases, cancels out.

The other equilibrium condition can be obtained if one expresses the electron pressure increment due to the electron density jump ( $\delta n_e = n_e^{\ell iq} - n_e^{sol}$ ) via that of the ion chemical potential. In particular,

$$P_e = - \frac{\partial E_e}{\partial V} = - \frac{E_e}{V} + n_e \varepsilon_{k_F} . \quad (20)$$

Hence,

$$\frac{dP_e}{dn_e} \delta n_e = n_e \frac{d\varepsilon_{k_F}}{dn_e} \delta n_e . \quad (21)$$

On the other hand,

$$\frac{d\Delta \mu_{1,2}}{dn_e} \delta n_e = Z_{1,2} \frac{d\varepsilon_{k_F}}{dn_e} \delta n_e . \quad (22)$$

Thus, subtracting the pressure equality condition (divided by  $n_e$ ) from the equality of the chemical potentials of the first ion species (divided by  $Z_1$ ), we arrive at the second equilibrium condition, in which the leading effect of the electron density jump is also removed:

$$\mu_1^{\ell iq} - \mu_1^{sol} - \frac{P_{BIM}^{\ell iq} - P_{BIM}^{sol}}{n_e/Z_1} = 0 . \quad (23)$$

In this case,  $P_{BIM}$  is the ion pressure in the mixture obtained by an appropriate differentiation of equation (7) or (12). All the quantities appearing in equations (19) and (23) should be calculated at one and the same electron density  $n_e$ .

In Fig. 1b, we illustrate conditions (19) and (23) by dashed (red) and solid (blue) lines, respectively. In particular, we consider an almost classic  $^{12}\text{C}/^{20}\text{Ne}$  mixture at  $n_e$ , corresponding to pure carbon at  $10^8 \text{ g cm}^{-3}$ , and at  $T = 0.8 T_{1m}^{\text{cl}}$ . This density is relatively low, so that ion quantum effects for carbon and neon are not yet pronounced.  $T_{1m}^{\text{cl}} = Z_1^{5/3} e^2 / (a_e \Gamma_m)$  is the melting temperature of the OCP, composed of the first ion species (i.e. carbon here), at given  $n_e$  and assuming classic Coulomb coupling strength at melting,  $\Gamma_m = 175.6$  (Baiko & Chugunov 2022). Furthermore, we used  $S_{\text{mixZ}}$  in equation (12) and  $\Delta f_{\text{nLM}}^{\text{sol}}$  parameterized as in Ogata et al. (1993).

Horizontal and vertical axes display neon fraction  $x_{\text{Ne}} = N_{\text{Ne}} / (N_{\text{Ne}} + N_{\text{C}})$  in the solid and in the liquid, respectively. One observes two intersection points (there is no intersection in the upper right corner), where both conditions are fulfilled simultaneously. For specified  $n_e$  and  $T$ , these points represent neon fractions, at which liquid and solid phases can co-exist. The locus of such points, obtained as  $T$  is varied, produces the phase diagram of the binary mixture at given density (cf. Fig. 6a).

Another important application of equations (19) and (23) is in finding boundaries of unstable solid domains, where a mechanical mixture of two solid solutions with different fractions of the constituents is preferable to a single solid solution. In order to accomplish this, one has to replace all quantities pertaining to the liquid in equations (19) and (23) by another set of solid quantities, parameterized by the second, independent heavier ion fraction  $x_2^{\text{sol}}$  (which would then appear in place of  $x_{\text{Ne}}^{\ell iq}$  in Fig. 1b). These solid solubility boundaries extend the phase diagram of a mixture to lower temperatures. At intermediate temperatures, they may (but do not have to) connect with melting/crystallization curves found at the previous step. By construction, in the present linear mixing formalism, one cannot establish dependence of the solid solubility boundaries on ion quantum effects. For that, one would need to know, in what way quantum effects modify  $\Delta f_{\text{nLM}}^{\text{sol}}$ , which would require new quantum first-principle studies.

Before proceeding to the results, let us remark, that equations (19) and (23) allow one to construct all possible double tangents to solid and liquid (or solid and solid) free energy curves (cf. Gordon 1968), including those that do not have real thermodynamic significance, i.e. do not correspond to free energy minima. When plotting phase diagrams, we have checked, that selected solutions did in fact minimized the free energy.

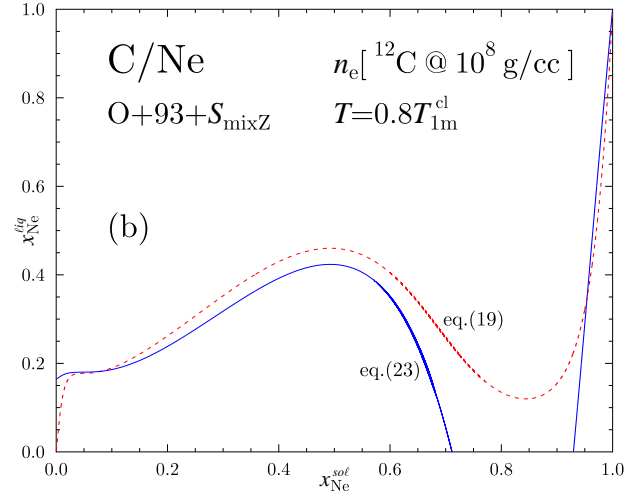
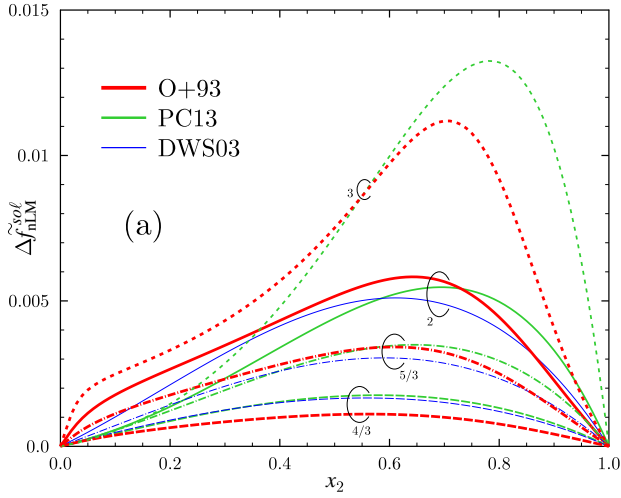


**Figure 1.** (a) Various parameterizations of  $\Delta f_{\text{nLM}}^{\text{sol}}$  (normalized to  $\Gamma_1$ ). Thick (red), thin (blue), and intermediate (green) curves show results of Ogata et al. (1993), DeWitt & Slattery (2003), and Potekhin & Chabrier (2013), respectively. Dashed, dot-dashed, solid, and short-dashed curves correspond to  $Z_2/Z_1 = 4/3, 5/3, 2$ , and  $3$ , respectively; (b) an example of simultaneous solution of equations (19) (dashed, red) and (23) (solid, blue) for an almost classic  $^{12}\text{C}/^{20}\text{Ne}$  mixture (see text for details).

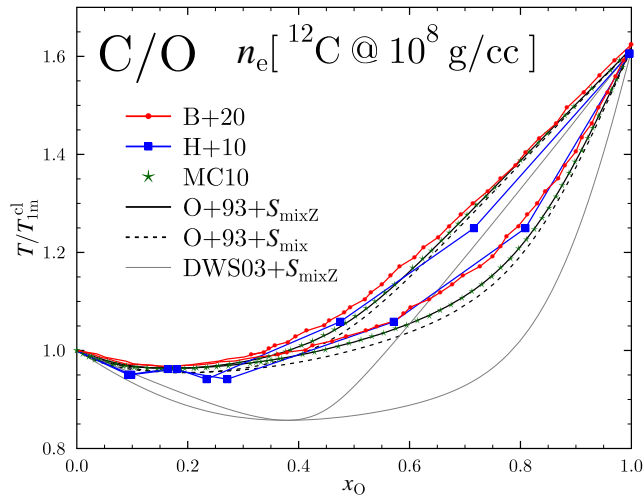


**Figure 2.** C/O phase diagram in the temperature-oxygen fraction plane at almost classic electron density corresponding to pure carbon at  $10^8 \text{ g cm}^{-3}$ . Curves and symbols represent different approaches to the diagram construction as detailed in the text.

## 5 PHASE DIAGRAMS

### 5.1 $^{12}\text{C}/^{16}\text{O}$ mixture

#### 5.1.1 State of the art

Let us apply the methods described in sections 2–4 to several specific mixtures anticipated in the interiors of degenerate stars. Of paramount importance is the carbon/oxygen mixture, which is believed to reside in the cores of a great number of intermediate-mass WD.

In Fig. 2, we illustrate state of the art. Curves and symbols of different types show phase diagrams obtained by different authors. The electron density is that of pure carbon at  $10^8 \text{ g cm}^{-3}$ , which is sufficiently low to render ion quantum effects not important. The temperature is measured in units of  $T_{1\text{m}}^{\text{cl}}$ , which (as before) is the classic melting temperature of pure carbon at this electron density.

There are several domains of interest in the temperature-oxygen fraction plane. The high-temperature region corresponds to a stable liquid mixture, the curve bounding it from below is called *liquidus*. In the same way, the low-temperature region represents a stable solid mixture, which is limited from above by the curve called *solidus*. Horizontal lines at intermediate temperatures cross the phase diagram at one or two pairs of points. These specify oxygen fractions in the liquid and in the solid, at which the phases can co-exist. The areas between the liquidus and solidus describe unstable zones, where matter can be viewed as a mechanical mixture of solid and liquid phases, whose compositions at a chosen temperature are given by the intersection points of solidus or liquidus with the respective horizontal line (cf. Gordon 1968).

Filled (red) circles display the most recent (classic) results for the C/O phase diagram obtained in Blouin et al. (2020) using the Gibbs-Duhem integration technique coupled to Monte Carlo simulations (GDMC). Slightly older molecular dynamics results by Horowitz et al. (2010) are shown by (blue) squares. Stars (green) show the results of Medin & Cumming (2010) obtained within the linear mixing with corrections framework as reproduced in Blouin et al. (2020). Medin & Cumming (2010) used classic OCP thermodynamics, corrections to linear mixing in the solid as fitted by Ogata et al. (1993), double-tangent construction, thermodynamic extrapolation, and  $S_{\text{mixZ}}$  as the residual entropy of the solid mixture.

The results of Medin & Cumming (2010) (stars) are in a perfect agreement with our solid (black) line. The latter is obtained under the same assumptions except that (i) the equilibrium conditions (19) and (23) are used in place of the double-tangent construction and (ii) the fitting expressions for the OCP thermodynamics (from Baiko et al. 2001; Potekhin & Chabrier 2000, and Baiko & Chugunov 2022 for harmonic solid, classic liquid, and quantum liquid and anharmonic solid terms, respectively) are utilized directly in the entire temperature range without invoking any extrapolation procedures. Dashes differ from the solid line by the

replacement  $S_{\text{mixZ}} \rightarrow S_{\text{mix}}$  in equation (12). The difference with the solid line is seen to be moderate, whereas the disagreement with the results of Blouin et al. (2020) becomes worse. Finally, the thin solid (grey) curve is obtained by the same method as the solid (black) one except that the parameterization of  $\Delta f_{\text{nLM}}^{\text{sol}}$  is taken from DeWitt & Slattery (2003). It is evident, that this result is in a more serious disagreement with the other curves than their mutual disagreement.

### 5.1.2 Miscibility gap and quantum effects

In Fig. 3, we extend the consideration to lower temperatures and higher densities to investigate the importance of ion quantum effects. The electron density in panel (a) corresponds to pure carbon at  $10^8 \text{ g cm}^{-3}$ , which is three orders of magnitude smaller than the density in panel (b). We do not consider densities higher than  $10^{11} \text{ g cm}^{-3}$ , because this would take us beyond the “stability strip”, and carbon would rapidly burn (e.g. Baiko 2021). Thick and thin curves assume the residual entropy of the solid equal to  $S_{\text{mixZ}}$  and  $S_{\text{mix}}$ , respectively. Different line types (and colors) refer to different parameterizations of  $\Delta f_{\text{nLM}}^{\text{sol}}$ : short-dashed (black) is for  $\Delta f_{\text{nLM}}^{\text{sol}} = 0$ , while solid (red), long-dashed (blue), and dot-dashed (green) represent parameterizations proposed by Ogata et al. (1993); DeWitt & Slattery (2003), and Potekhin & Chabrier (2013), respectively.

Regarding the already familiar liquid-solid structure (discussed in connection with Fig. 2), several further conclusions can be made. While for  $\Delta f_{\text{nLM}}^{\text{sol}} = 0$  this part of the diagram is of the spindle type, the three non-zero variants of  $\Delta f_{\text{nLM}}^{\text{sol}}$  produce azeotropic structures. The diagram based on  $\Delta f_{\text{nLM}}^{\text{sol}}$  due to Ogata et al. (1993) is much closer to the results of GDMC studies (cf. Fig. 2) being qualitatively different from the diagrams based on  $\Delta f_{\text{nLM}}^{\text{sol}}$  due to the other authors. The difference between predictions based on fits of DeWitt & Slattery (2003) and Potekhin & Chabrier (2013) is moderate. Use of  $S_{\text{mix}}$  in place of  $S_{\text{mixZ}}$  results in a moderate shift of the curves to lower temperatures with their endpoints fixed at OCP melting temperatures. Ion quantum effects for this mixture are seen to result in a stretch of the liquid-solid structure associated with the fact that, for pure carbon (left-hand edge of the diagram), quantum effects at the chosen density are already sufficiently pronounced to reduce the melting temperature below its classic value. Liquid-solid unstable domains for parameterizations of DeWitt & Slattery (2003) and Potekhin & Chabrier (2013) cover noticeably more area at higher density (which means stronger separation of species upon crystallization), while dot-dashed (green) solidus for  $0.4 \lesssim x_{\text{O}} \lesssim 0.8$  is somewhat flatter.

In addition to the liquid-solid structure, a lower-temperature solid-solid structure exists. Instead of a single stable solid solution, we actually obtain a rather extensive unstable domain, where a mechanical mixture of two solids is thermodynamically preferable. Such regions are well-known in many terrestrial materials (e.g. section 4.14 in Gordon 1968) and are called *miscibility gaps* (MG). The curve bounding a MG is called *solvus*. The compositions of the two solid solutions at a chosen temperature are given by the intersection points of the solvus with the respective horizontal line.

Clearly, solvus is very sensitive to a particular expression for  $\Delta f_{\text{nLM}}^{\text{sol}}$ , and the fits of DeWitt & Slattery (2003) and Potekhin & Chabrier (2013) generate really large MG. By contrast, the residual entropy has almost no effect on MG. The solvi shown in panels (a) and (b) are the same, because, as mentioned in section 4, one cannot establish MG dependence on ion quantum effects in the present formalism.

## 5.2 $^{16}\text{O}/^{20}\text{Ne}$ mixture

The oxygen/neon mixture is believed to occur in the cores of massive WD. In this case, the ratio  $Z_2/Z_1 = 5/4$  is closer to 1 than for the C/O mixture, hence, one anticipates a qualitatively similar but less “developed” picture as for the latter. In Fig. 4, we plot phase diagrams for this mixture. Panel (a) corresponds to the same electron density as in Fig. 3a for the C/O mixture, whereas quantum effects in panel (b) are illustrated at an order of magnitude higher electron density (for the sake of the illustration, we neglect neutronization and any other effects which may render such physical conditions unachievable). In view of the smaller charge ratio, the range of temperatures, at which liquid and solid phases with different fractions of constituents co-exist, is smaller than for C/O. Quantum effects in panel (b) are less pronounced for heavier and stronger charged oxygen ions than for carbon ions in Fig. 3b. This is because the ion plasma temperature scales as  $\sqrt{n_e}$ , i.e. for oxygen at  $10^{12} \text{ g cm}^{-3}$  it is  $\sim 3.2$  times greater than for carbon at  $10^{11} \text{ g cm}^{-3}$ . However, the melting temperature behaves as  $Z_1^{5/3} n_e^{1/3}$ , and it is  $\sim 3.5$  times greater for oxygen than for carbon. Accordingly,  $T/T_p$  is greater in Fig. 4b, and this system is less quantum.

Even though  $Z_2/Z_1 = 5/4 = 15/12$  is not much smaller than  $4/3 = 16/12$ , the effect on MG is profound. Regardless of the  $\Delta f_{\text{nLM}}^{\text{sol}}$  fit, MG for O/Ne are greatly reduced in comparison with C/O. In particular, the maximum gap temperature for the fit of Ogata et al. (1993) is just  $0.27T_{1\text{m}}^{\text{cl}}$  for O/Ne, whereas for C/O it reaches  $0.49T_{1\text{m}}^{\text{cl}}$ .

## 5.3 Miscibility gaps and white dwarf cooling

The occurrence and properties of the miscibility gaps in Figs. 3 and 4 may have important implications for WD cooling theory. Let us note first, that the appearance of MG is rather robust. With increase of  $Z_2/Z_1$ , they grow and eventually collide with the liquid-solid structure, morphing, in a natural way, into two-solid regions of eutectic phase diagrams prevailing there (cf. Fig. 5). Presence of MG does not rely on thermodynamic fit extrapolations, as both components are below their solidification temperatures, and only formulae for solids are used. The gaps are very sensitive to composition and constitutive physics, being significantly different for C/O and O/Ne mixtures and for different parameterizations of  $\Delta f_{\text{nLM}}^{\text{sol}}$  (cf. Figs. 3 and 4).

Cooling through MG is similar to cooling through the usual liquid-solid two-phase region (e.g. section 4.15 in Gordon 1968). On reaching the solvus curve, a single stable solid solution, prevailing at higher temperatures, becomes saturated with a second solid solution, whose composition is determined by the other intersection of the solvus with the horizontal (constant temperature) line, and exsolution takes place. Upon further cooling, the two solutions move

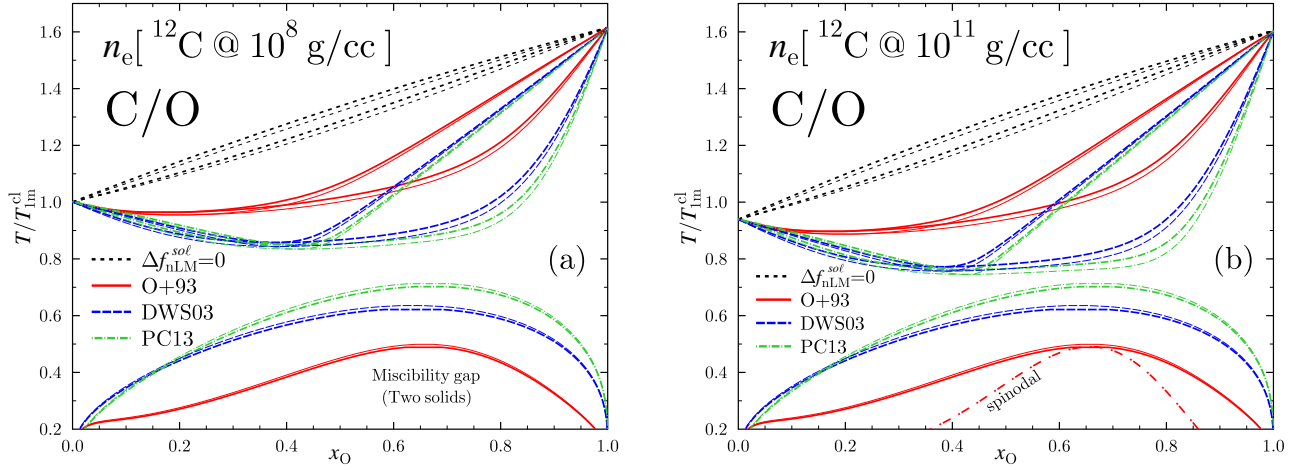


**Figure 3.** C/O phase diagram calculated in this work using different fits for  $\Delta f_{\text{nLM}}^{\text{sol}}$ :  $\Delta f_{\text{nLM}}^{\text{sol}}=0$  (short-dashed, black), Ogata et al. (1993) (solid, red), DeWitt & Slattery (2003) (long-dashed, blue), and Potekhin & Chabrier (2013) (dot-dashed, green); different solid mixture residual entropies:  $S_{\text{mixZ}}$  (thick) and  $S_{\text{mix}}$  (thin); and different electron densities: almost classic (a) and moderately quantum (b). Dot-dash-spaced line shows spinodal for O+93+ $S_{\text{mixZ}}$ , same for both densities.

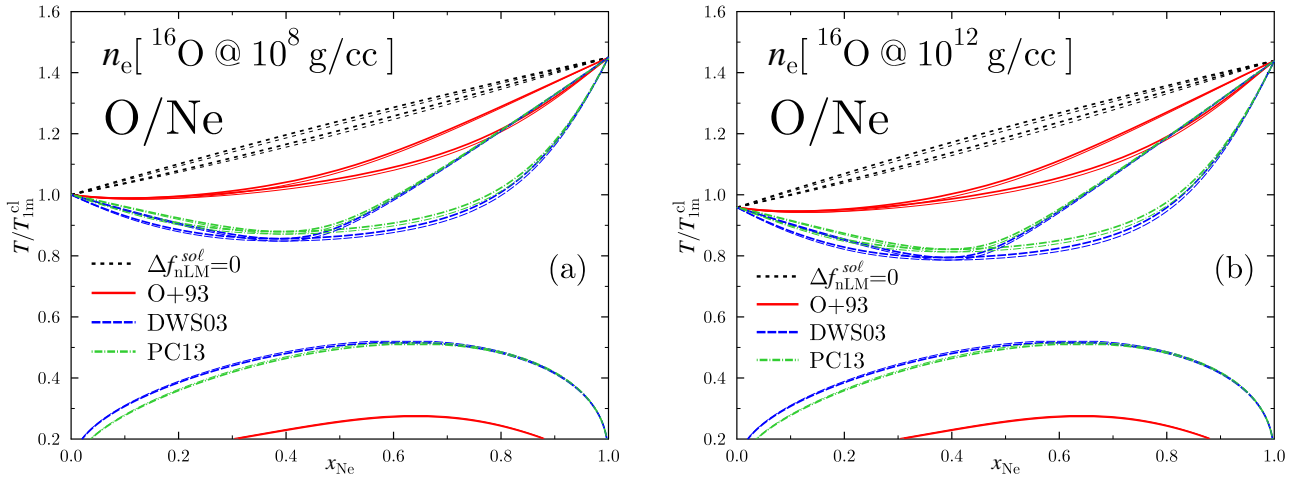


**Figure 4.** Same as in Fig. 3 but for O/Ne mixture, and the electron density in panels (a) and (b) corresponds to pure oxygen at  $10^8$  and  $10^{12} \text{ g cm}^{-3}$ , respectively.

down along the solvus branches, their relative fractions being determined by the lever rule. Such exsolution process in a solid phase is well-known on Earth, where it can result in a formation of microscopic to megascopic lamellae.<sup>1</sup>

Whether a separation of  $Z_1$ - and  $Z_2$ -rich solutions does happen in dense crystallized interior of compact stars is an open question. In principle, Coulomb crystals are in many respects similar to strongly-coupled Coulomb liquids, for which such a rearrangement would not raise any objections. In both cases, the stress tensor is dominated by the pressure of degenerate electron gas, whose energy density is huge in comparison with any Coulomb contribution responsible for structure. The jumps of thermodynamic and kinetic properties at crystallization are not large (e.g. Baiko et al. 1998; Baiko & Chugunov 2022) and eigenmodes of Coulomb solids and liquids are alike (e.g. Ott et al. 2013). Thus, it almost

looks as if the separation of species with a formation of some geometric (e.g. lamellar) superstructure in these peculiar crystals in dense matter should proceed easier (with lower barriers) than in terrestrial materials. Just like on Earth, the transformation could be intensified by a finite amount of undercooling, which helps overcome size and compositional barriers. This would make the effective gaps more narrow, which can be described as a replacement of the equilibrium solvus curves in Figs. 3 and 4 by spinodal ones (e.g. section 4.15 in Gordon 1968).

Turning back to WD cooling, if the lamellae have a tendency of forming perpendicular to the gravity, then, in a slab of stellar material, we expect accumulation of the heavier ( $Z_2$ -rich) solution at the bottom. This would lead to an energy release. For megascopic lamellae, the released energy may be large, because the process involves the bulk of the core material, or, at least, those regions, where the initial solid composition is such that it hits the MG with decrease of temperature. This last consideration also governs selectivity of the phenomenon: if, for instance, the composition after

<sup>1</sup> see e.g. megascopic antiperthite here: <https://en.wikipedia.org/wiki/Perthite>

crystallization in a C/O WD lies beyond the spinodal curve in Fig. 3, the exsolution would not operate as effectively or at all.

Naturally, the exsolution in a chunk of stellar material may occur only after its crystallization is complete. As we have already mentioned, the proximity of MG to the solidus is subject to theoretical uncertainty and is sensitively regulated by matter composition. For instance, the situation is very different in C/O and O/Ne WD, because the gaps occur at significantly higher temperatures in the former. The maximum gap temperature may actually be closer to the crystallization region, because the simplest linear-mixing prescription of section 3 may underestimate the actual gaps due to possible formation of compoundlike structures (cf. Fig. 6.2 in Gordon 1968) known as binary ionic crystals (e.g. Kozhberov & Baiko 2015). Furthermore, ion quantum effects tend to bring solidus closer to the solvus at high densities. Given composition, the exsolution starts operating earlier in more massive stars, which reach relevant temperatures faster. Under certain assumptions, the exsolution in central parts of the core may be concurrent with solidification of its outer regions.

Summarizing, the MG in C/O and O/Ne mixtures may be responsible for substantial reservoirs of gravitational energy in cooling WD. We encourage WD modellers to include MG in future cooling simulations under various assumptions regarding maximum gap temperature, width, and lamella geometry in order to see if any of these parameters can be constrained experimentally.

#### 5.4 Varying $Z_2$

In this subsection, we analyze mixtures, which are characterized by a gradually increasing charge ratio. This allows one to investigate the evolution of the binary ionic mixture phase diagram with this parameter (regardless of the practical relevance of considered compositions). In all cases, we assume  $Z_1 = 6$ , and mass numbers equal to double charge numbers ( $A_{1,2} = 2Z_{1,2}$ ).

In Fig. 5, there are 12 panels, corresponding to mixtures with  $Z_2$  varying from 8.7 to 12. In all cases, the electron density is that of pure carbon at  $\rho = 10^8 \text{ g cm}^{-3}$ , so that the systems are essentially classic. Parameterization of  $\Delta f_{\text{nLM}}^{\text{sol}}$  from Ogata et al. (1993) is used. Residual entropy of the solid mixture is taken as  $S_{\text{mixZ}}$ . Horizontal axes display the fractions of respective  $Z_2$ -constituents,  $x_2 = N_2/(N_1 + N_2)$ , vertical axes show temperature in units of  $T_{\text{lm}}^{\text{cl}}$ .

Phase diagrams are comprised of curves of three different types: solid (blue), dashed (red), and dotted (cyan). Dashed and solid curves determine boundaries of liquid and crystal phases, i.e. these are liquidus and solidus, respectively. Dotted curves are obtained by solving equations (19) and (23) applied to de-mixing in the solid phase, i.e. they represent solvi.

A liquid mixture with a particular composition and temperature, corresponding to a point on a liquidus, can co-exist with only one solid mixture, corresponding to a point at the same temperature on the associated solidus (cf. Fig. 1b). If two or more pairs of solid and dashed curves exist at a given temperature, one can establish the association between them based on continuity, smoothness, and the fact that associated curves span the same temperature

range. Likewise, solvus can be split into pairs of associated branches, and a point on a particular solvus branch represents a solid mixture, which can co-exist with another solid mixture with a different composition given by a point at the same temperature on the associated solvus branch.

In the first panel of Fig. 5,  $Z_2 = 8.7$ , one sees an azeotropic phase diagram with the MG reaching fairly high temperatures, which has developed in a straightforward manner from the thick solid (red) line in Fig. 3a (for  $Z_2 = 8$ ). At  $Z_2 = 8.9$ , the high- and low-temperature structures have already merged. The diagram exhibits a  $\Lambda$ -like feature (at  $x_2 \approx 0.52$ ) and an invariant reaction of the peritectic type:  $L + \beta \rightarrow \alpha$ . This state continues past  $Z_2 = 9$  and includes O/Mg mixture. By  $Z_2 \approx 9.3$ , the diagram becomes eutectic (the eutectic point is given by the intersection of the two dashed curves or by the tip of the V-feature at  $x_2 \approx 0.38$ ) with the standard eutectic invariant reaction  $L \rightarrow \alpha + \beta$  and with a rather large allowed fraction of the heavier element in a crystal made of the lighter species ( $x_2 \lesssim 0.36$ ).

This state continues till  $Z_2 \sim 9.8$ , where a second MG appears at low  $x_2$ . For C/Ne, the MG barely clears the liquid-solid structure, crashing into it at  $Z_2 \sim 10.1$ . For a narrow range of charge ratios, this makes the diagram very complex with as many as three invariant regions<sup>2</sup> (for peritectic and eutectic phase diagrams, invariant regions are shown by thin horizontal lines). Stable solid domain at low  $x_2$  splits into two. One of them ( $\alpha$ ) corresponds to an almost pure crystal made of the lighter element. It is characterized by gradually decreasing maximum  $x_2$  and it survives till much higher  $Z_2$ , including C/Mg mixture at  $Z_2 = 12$ . The other ( $\gamma$ ) is short-lived. It is represented by a diminishing island, which is last seen at  $Z_2 \sim 10.3$ .

Starting from  $Z_2 \sim 10.5$ , the diagram assumes a chrestomathic eutectic shape. Near the eutectic point, the right-hand section of the liquidus demonstrates a tendency to steepening, which, by  $Z_2/Z_1 = 3$ , results in a breaking of the liquidus and transformation to a diagram with a liquid gap (see section 5.6).

If  $S_{\text{mixZ}} \rightarrow S_{\text{mix}}$  in equation (12), the sequence of phase diagrams remains nearly the same as in Fig. 5, but the respective shapes occur at  $Z_2$ , which are  $\sim 0.1$  smaller than in Fig. 5. In particular, there are two separate stable solid domains at low  $x_2$  for C/Ne mixture with  $S_{\text{mix}}$ , looking very similar to  $Z_2 = 10.1$  graph in Fig. 5 (see Fig. 6a).

#### 5.5 $^{12}\text{C}/^{20}\text{Ne}$ and $^{12}\text{C}/^{24}\text{Mg}$ mixtures

The results for carbon/neon mixture are displayed in more detail in Fig. 6. Electron densities, type, and colour of the curves are the same as in Fig. 3, so that panel (a) corresponds to classic, while panel (b) to moderately quantum densities. Grey horizontal lines display eutectic invariant regions for various  $\Delta f_{\text{nLM}}^{\text{sol}}$  parameterizations and residual entropies. To avoid cluttering, we do not extend dashed and dot-dashed curves below their eutectic points in panel (a) and do not show respective invariant regions. These features would look exactly the same as in panel (b).

<sup>2</sup> for binary systems, invariant regions are phase diagram regions, where the number of different phases co-existing in equilibrium is three



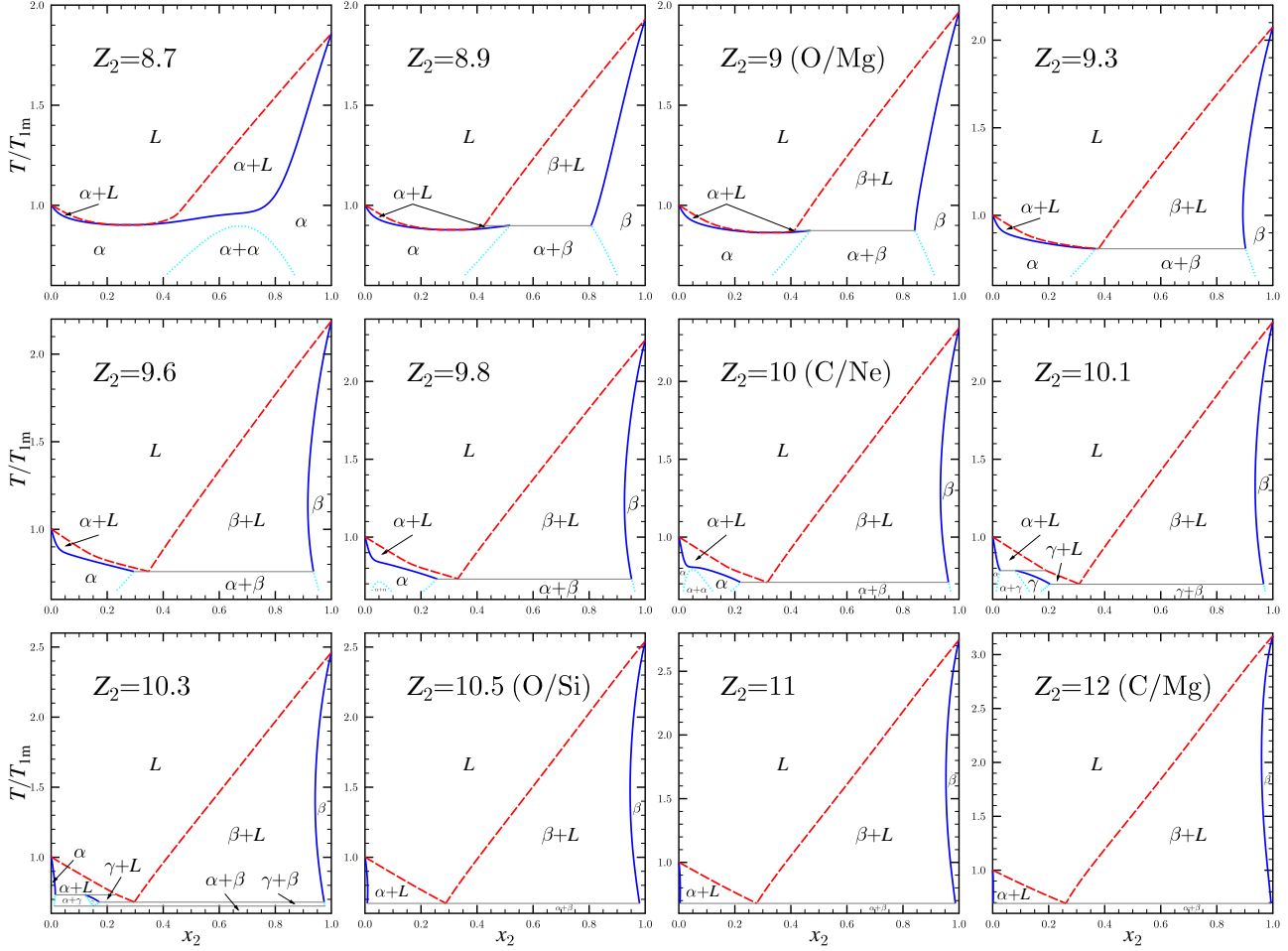


**Figure 5.** Phase diagrams for classic mixtures with  $Z_1 = 6$ , varying  $Z_2$ , and  $A_{1,2} = 2Z_{1,2}$ . Solidus and liquidus are shown by solid (blue) and dashed (red) curves, respectively. Dotted (cyan) curves outline solid solubility limits. ‘L’ marks liquid domains; ‘ $\alpha$ ’, ‘ $\beta$ ’, and ‘ $\gamma$ ’ represent three different solid solutions. ‘+’ sign indicates unstable zones, where a mechanical mixture of two solutions is preferable. Thin horizontal lines correspond to invariant regions in peritectic and eutectic systems.

In section 5.4, we have already discussed the complex low- $x_{\text{Ne}}$  corner of the phase diagram for the Ogata et al. (1993) fit in panel (a). Remarkably, the “complexity” disappears in panel (b). As we have mentioned, the solid solubility curves are not affected by ion quantum effects. Hence, the reason for the change is a “consumption” of the two-solid region by the liquid-solid structure moving to lower temperatures due to ion quantization. As a result, for  $x_{\text{Ne}} \lesssim 0.3$  in panel (b), the free energy minimum is realized by a solid solution with an extremely low neon fraction, a liquid solution, or a mechanical mixture of the two. The thick solid (red) curve in “quantum” panel (b) thus achieves a more advanced degree of transformation to the eutectic type, looking similar to the classic mixture diagram at  $Z_2 = 10.5$  in Fig. 5.

An important conclusion is that, for some charge ratios, rather mild ion quantum effects, considered in this work, may result in a qualitative modification of the phase diagram. Same goes for the residual entropy choice as illustrated by thick and thin solid (red) curves in Fig. 6a. In particular, quantum effects are expected to modify the low- $x_{\text{Ne}}$  and low- $x_{\text{O}}$  corner of the ternary C/O/Ne phase diagram at high densities (cf. Fig. 4a of Caplan et al. 2020). This may

be relevant for the outcome of  $^{22}\text{Ne}$  distillation invoked for an explanation of observed cooling delays of ultramassive WD (Blouin et al. 2021).

The other  $\Delta f_{\text{nLM}}^{\text{sol}}$  parameterizations produce quantitatively similar to each other, standard looking eutectic phase diagrams, in which neon fraction in a carbon crystal can exceed 20% but carbon fraction in neon crystals is quite low (especially for the fit of Potekhin & Chabrier 2013). The only quantum effect that can be seen for these  $\Delta f_{\text{nLM}}^{\text{sol}}$  expressions is a reduction of the pure carbon melting temperature and an associated reduction of the eutectic temperatures.

Before proceeding further, let us make a technical note. In Fig. 6, for  $\Delta f_{\text{nLM}}^{\text{sol}} = 0$  phase diagram, there is a noticeable distortion of the spindle near its upper right corner. It is associated with higher order crystal anharmonic corrections employed at rather low  $\Gamma < \Gamma_{\text{m}}$ . We try to elucidate this effect in Fig. 7a for carbon/magnesium mixture. In this case, thick (black) and thin (magenta) solid curves display phase diagrams for  $\Delta f_{\text{nLM}}^{\text{sol}} = 0$  assuming full equations for crystal thermodynamics (with classic anharmonic coefficients  $A_{2,3\text{cl}}$  as reported in Baiko & Chugunov 2022) and assuming  $A_{2,3\text{cl}} = 0$  (as suggested earlier by Medin & Cumming

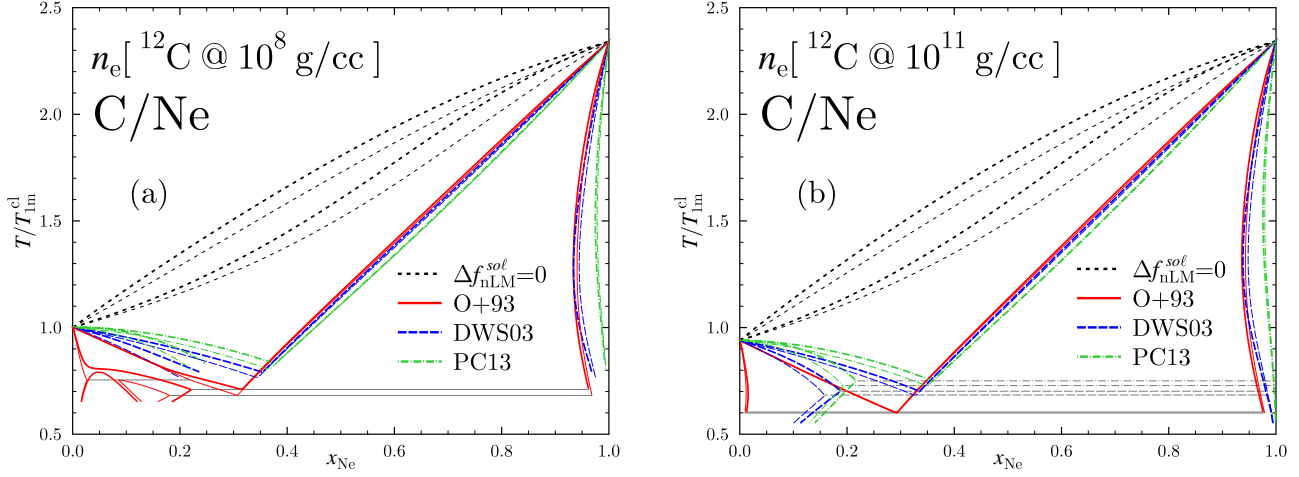


**Figure 6.** Same as in Fig. 3 but for C/Ne mixture. Grey horizontal lines display eutectic invariant regions. For clarity, dashed and dot-dashed curves are not shown in panel (a) below their eutectic points. They would look exactly the same as in panel (b).

2010), respectively. Nulling  $A_{2,3cl}$  also slightly affects melting points for both pure carbon and pure magnesium crystals. Dashed curves assume  $S_{mix}$  for the residual entropy. For  $Z_2/Z_1$  considered so far, we have been checking the robustness of our conclusions against setting  $A_{2,3cl}$  to zero and have observed no issues.

In Fig. 7b, we show C/Mg phase diagrams for  $\Delta f_{nLM}^{sol} \neq 0$ . Thick curves correspond to a classic system, whereas thin ones illustrate ion quantum effects. The latter are seen to be mild. They do not produce qualitative changes for this charge ratio. We kept  $A_{2,3cl}$  to their original values; setting them to 0 results in a slight, almost uniform shift of the phase diagrams down related to the reduction of melting temperatures for both pure crystals. The general shape of the phase diagram and the effect of different  $\Delta f_{nLM}^{sol}$  parameterizations are virtually the same as for already discussed quantum C/Ne mixture.

Summarizing, in contrast to systems with a smaller charge ratio, C/Ne and C/Mg mixtures, for  $\Delta f_{nLM}^{sol} \neq 0$ , exhibit phase diagrams of the eutectic type. These contain two widely separated solid domains, enriched in lighter or heavier ion species. At  $x_{Ne} \sim 0.25 - 0.35$ , there is a eutectic point, below which liquid does not exist. Cooling in eutectic systems is known to be accompanied by interesting nonequilibrium phenomena (e.g. section 6 of Gordon 1968). In general, depending on the initial composition of a cooling liquid, the liquidus can be reached to the left or to the right of the eutectic point. This will cause precipitation of, respectively,  $Z_1$ - or  $Z_2$ -rich solids called primary solidification. Further cooling will proceed along the liquidus. If the initial composition is such that the eutectic point can be reached during this process, the liquid will completely freeze, separating into  $Z_1$ - and  $Z_2$ -rich crystallites. However, through the effect known as constitutional undercooling, a quasi-periodic lamellar superstructure may actually form. This, along with the primary grains, affects the overall crystal strength and disorder and may be important for elastic, kinetic, and other properties of these layers.

### 5.6 $^4\text{He}/^{12}\text{C}$ mixture

Finally, let us briefly describe a phase diagram for a mixture with a rather large  $Z_2/Z_1 = 3$ . We shall analyze this case using the example of helium/carbon mixture, which is relevant for accreting WD. The results should be indistinguishable if any other  $Z_1$  is used, provided the densities are rescaled appropriately to achieve the same strength of ion quantum effects. For this charge ratio, the  $\Delta f_{nLM}^{sol}$  fit by DeWitt & Slattery (2003) is beyond its applicability limits. Hence, we only consider parameterizations by Ogata et al. (1993) and Potekhin & Chabrier (2013), assuming  $A_{2,3cl} = 0$  (cf. section 5.5).

In Fig. 8a, the phase diagram based on the fit by Ogata et al. (1993) is shown for several electron densities. One observes two main structures. First, there is a large unstable “triangle” at intermediate and large  $x_C$  reminiscent of eutectic phase diagrams at lower  $Z_2/Z_1$ . On top and to the left of it, there is a stable liquid domain. To the right of the triangle, there is a narrow stable solid region, where helium fraction must stay below 5%. Solid and dashed curves have the residual solid mixture entropy equal to  $S_{mixZ}$  and  $S_{mix}$ , respectively. Two solid lines (merging for  $x_C > 0.45$ ) are plotted for different electron densities. (Same applies to two merging dashed lines.) The outer solid (or dashed) line assumes the electron density of pure helium at  $10^5 \text{ g cm}^{-3}$ , the inner one  $10^7 \text{ g cm}^{-3}$ . We have also checked  $10^8$  and  $10^9 \text{ g cm}^{-3}$ , which resulted in a further minuscule inward motion of these curves.

At low  $x_C$ , there is another structure which should be analyzed together with the curves shown in the inset. Five curves from top to bottom represent liquidus for electron densities corresponding to pure helium at  $10^5$ ,  $10^6$ ,  $3 \times 10^6$ ,  $6 \times 10^6$ , and  $10^7 \text{ g cm}^{-3}$ , respectively. The associated solidi are shown in the inset. One observes an extremely narrow stable sector of an almost pure helium crystal with a carbon admixture not exceeding a few times  $10^{-4}$ . With density increase, the allowed carbon fraction steadily drops. We have also considered higher electron densities. The reduction of the structure continued, and it was not seen in the scale of Fig. 8a already at  $10^8 \text{ g cm}^{-3}$ .

One sees that, at no density, the two structures inter-

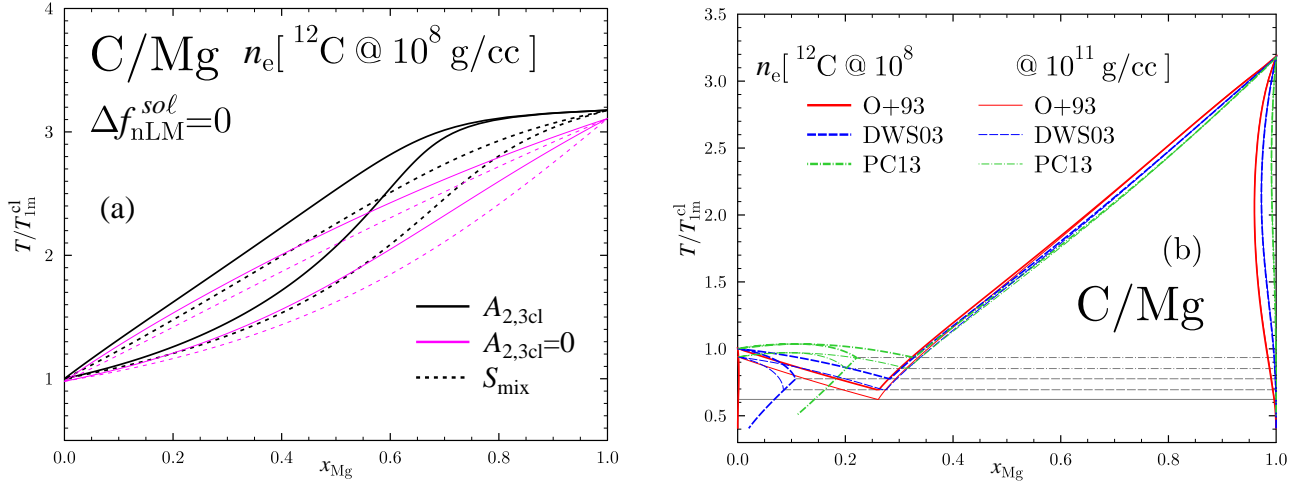


**Figure 7.** Phase diagram for C/Mg mixture. (a) Classic mixture with  $\Delta f_{\text{nLM}}^{\text{sol}} = 0$ . Solid thick (black) and thin (magenta) curves display calculations with full  $A_{2,3\text{cl}}$  in the solid phase and with  $A_{2,3\text{cl}} = 0$ , respectively. Dashed curves are obtained from the solid ones by replacement  $S_{\text{mixZ}} \rightarrow S_{\text{mix}}$ . (b) Thick and thin curves correspond to classic and quantum densities, respectively, with  $\Delta f_{\text{nLM}}^{\text{sol}}$  given by fits of Ogata et al. (1993) (solid, red), DeWitt & Slattery (2003) (dashed, blue), and Potekhin & Chabrier (2013) (dot-dashed, green). Horizontal lines are invariant regions.

sect, no eutectic point forms, and a stable liquid solution between the unstable regions is predicted to exist down to very low temperatures. The liquid gap becomes wider as ion quantum effects become stronger (i.e. as the density increases). Of course, the calculations become less and less reliable with decrease of temperature, because liquid fits are used well below crystallization.

In panels (b) and (c) of Fig. 8, we show phase diagrams based on  $\Delta f_{\text{nLM}}^{\text{sol}}$  fit proposed by Potekhin & Chabrier (2013) with the residual entropy equal to  $S_{\text{mixZ}}$  and  $S_{\text{mix}}$ , respectively. The general features of these phase diagrams are similar to the diagram shown in panel (a). In particular, there is a triangular unstable region at  $x_{\text{C}} \gtrsim 0.3$ , whose boundaries are weakly sensitive to the density. In contrast to panel (a), very low fraction of helium ( $< 0.0005$ , see the inset, where all 5 curves have merged) is predicted in almost pure stable carbon crystals.

In the low- $x_{\text{C}}$  region, the diagram in panel (b) has a narrow spindle-shaped unstable area, below and to the right of which a helium crystal with a rather large fraction of carbon (up to  $\sim 25\%$  at classic densities) is predicted. The maximum carbon fraction decreases as the system becomes more quantum. The crystal domain is bounded from the right by another unstable zone, whose right boundary (liquidus) may intersect liquidus of the large- $x_{\text{C}}$  unstable region. This leads to a formation of a eutectic point and an extensive two-solid unstable region. However, as ion quantum effects get stronger, the two structures cease intersecting, and a liquid gap between them, similar to the one in panel (a), appears.

If the residual entropy is equal to  $S_{\text{mix}}$  (panel c), the diagram is very similar to panel (b). However, the spindle-shaped unstable zone is degenerated, and the maximum fraction of carbon in a helium-dominated crystal does not exceed  $\sim 15\%$ .

## 6 CONCLUSION

We have studied phase diagrams of binary ionic mixtures in the  $1 < Z_2/Z_1 \leq 3$  range using the linear mixing with corrections approach and taking advantage of the recent progress in understanding quantum OCP thermodynamics. We have compared three fits for corrections to linear-mixing energies in the solid phase and two different models of solid residual entropy at  $T = 0$ . We have used actual fits of OCP thermodynamic functions in the entire required  $\Gamma$  ranges, including, where needed, solid phase formulae at temperatures above melting and vice versa, without resorting to any extrapolation schemes. This is the least reliable aspect of BIM thermodynamic calculations based on the linear mixing theory. It can be improved via first-principle analysis of the mixtures. Our results for the C/O phase diagram at classic conditions with non-linear-mixing corrections given by Ogata et al. (1993) and with the standard choice for the solid residual entropy agree well with previous work (Medin & Cumming 2010; Blouin et al. 2020).

For solid C/O and O/Ne mixtures, we have discovered extensive miscibility gaps. Their appearance seems to be a robust feature of the theory: the gaps evolve naturally into two-solid regions of eutectic phase diagrams predicted at higher  $Z_2/Z_1$  and also they do not rely on fit extensions beyond applicability limits because both components are solid. The gaps are very sensitive to BIM composition and physics being strongly different for C/O and O/Ne mixtures and for the three variants of the  $\Delta f_{\text{nLM}}^{\text{sol}}$  fit.

When matter cools to its miscibility gap temperature, the exsolution process (well-known on Earth) starts taking place. It results in a separation of heavier and lighter ( $Z_2$ - and  $Z_1$ -rich) solid solutions, which may represent a significant reservoir of gravitational energy. It would be interesting to include this effect in future WD cooling simulations.

At higher  $Z_2/Z_1$ , our analysis indicates a transformation of azeotropic phase diagrams into peritectic and eventually to eutectic ones. Cooling and freezing in such systems may result in a precipitation of  $Z_1$ - or  $Z_2$ -rich solids.

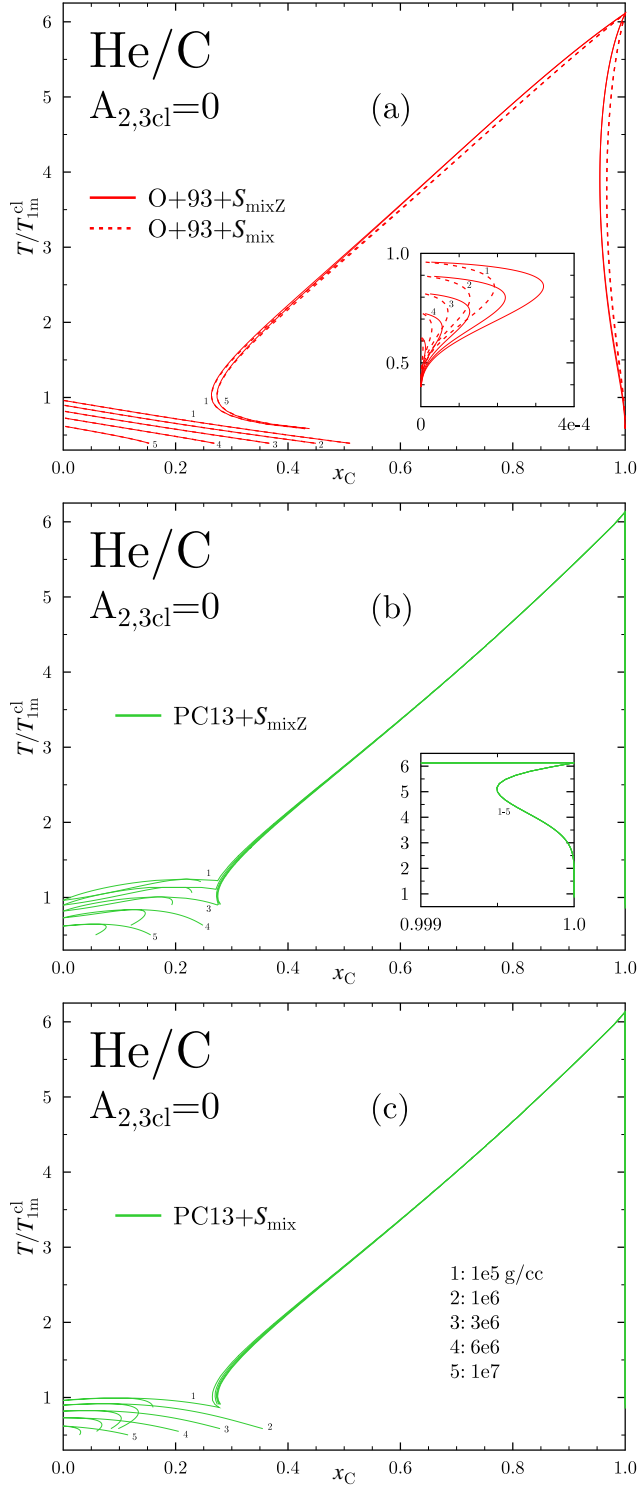


**Figure 8.** He/C phase diagram for  $\Delta f_{\text{nLM}}^{\text{sol}}$  given by Ogata et al. (1993) (panel a); Potekhin & Chabrier (2013) with  $S_{\text{mixZ}}$  (panel b); Potekhin & Chabrier (2013) with  $S_{\text{mix}}$  (panel c). Solid and dashed curves in panel (a) correspond to calculations with  $S_{\text{mixZ}}$  and  $S_{\text{mix}}$ , respectively. Curves marked by numerals 1–5 illustrate ion quantum effects and correspond to different electron densities listed in the legend in panel (c).

A nonequilibrium effect of constitutional undercooling may produce quasi-periodic superstructures of various geometries. All these processes affect crystal strength, kinetics, and other important properties of matter.

Ion quantum effects, for the most part, result in moderate modifications of phase diagrams, which can be traced back to melting temperature decrease in quantum one-component systems. However, for certain charge ratios, a BIM may be close to a qualitative transformation of its phase diagram, in which case ion quantum effects may produce drastic restructuring of the latter (e.g. Fig. 6). This is expected to affect also the low- $x_{\text{Ne}}$  and low- $x_{\text{O}}$  corner of the ternary C/O/Ne phase diagram at high densities, which may be relevant for the outcome of  $^{22}\text{Ne}$  distillation process in ultramassive WD.

In general, phase diagrams constructed for non-zero corrections to solid-phase linear-mixing energies exhibit much stronger separation of ionic species upon mixture crystallization than those in the model without corrections, especially at  $Z_2/Z_1 \gtrsim 1.5$ . The separation obtained from fits of DeWitt & Slattery (2003) and Potekhin & Chabrier (2013) is noticeably greater than that stemming from the parameterization by Ogata et al. (1993) for smaller charge ratios (such as O/Ne or C/O mixtures). For eutectic systems, these two groups of fits differ quite a bit in terms of stable solid solution compositions and eutectic point positions. The question of which of these results is closer to the reality can be settled via first-principle analysis. The most recent classic GDMC study of Blouin et al. (2020) for C/O mixture indicates that the fit of Ogata et al. (1993) is likely closer to the truth at this charge ratio.

We have found only rather weak sensitivity to the residual entropy choice across the parameter space. For C/O mixture, replacing  $S_{\text{mixZ}} \rightarrow S_{\text{mix}}$  worsens the agreement with the curves reported by Blouin et al. (2020) (Fig. 2).

We anticipate our results to enable more reliable modelling of ion redistribution at melting/crystallization and after it, gravitational energy release, thermodynamics, kinetics, elasticity etc in a variety of astrophysical phenomena associated with compact stars.

## ACKNOWLEDGMENTS

This work, except for subsection 5.3, was supported by RSF grant 19-12-00133-P. The author is grateful to A. I. Chugunov for discussions at the initial stages of this work and for useful critique of the manuscript. The author is deeply thankful to anonymous referee for valuable remarks.

## DATA AVAILABILITY

The data underlying this article will be shared on reasonable request to the author.

## REFERENCES

- Baiko D. A., 2019, MNRAS, 488, 5042
- Baiko D. A., 2021, MNRAS, 508, 2134
- Baiko D. A., Chugunov A. I., 2022, MNRAS, 510, 2628

- Baiko D. A., Kaminker A. D., Potekhin A. Y., Yakovlev D. G., 1998, *Phys. Rev. Lett.*, 81, 5556
- Baiko D. A., Potekhin A. Y., Yakovlev D. G., 2001, *Phys. Rev. E*, 64, 057402
- Baiko D. A., Yakovlev D. G., 2019, *MNRAS*, 490, 5839
- Bauer E. B., Schwab J., Bildsten L., Cheng S., 2020, *ApJ*, 902, 93
- Blouin S., Daligault J., 2021, *Phys. Rev. E*, 103, 043204
- Blouin S., Daligault J., Saumon D., 2021, *ApJL*, 911, L5
- Blouin S., Daligault J., Saumon D., Bedard A., Brassard P., 2020, *A&A*, 640, L11
- Camisassa M. E., Althaus L. G., Torres S., Córscico A. H., Rebassa-Mansergas A., Tremblay P.-E., Cheng S., Raddi R., 2021, *A&A*, 649, L7
- Caplan M. E., 2020, *Phys. Rev. E*, 101, 023201
- Caplan M. E., Horowitz C. J., Cumming A., 2020, *ApJL*, 902, L44
- Cheng S., Cummings J. D., Ménard B., 2019, *ApJ*, 886, 100
- Daligault J., Gupta S., 2009, *ApJ*, 703, 994
- DeWitt H., Slattey W., 2003, *Contrib. Plasma Phys.*, 43, 279
- Fantina A. F., De Ridder S., Chamel N., Gulminelli F., *A&A*, 633, A149
- Flowers E., Itoh N., 1976, *ApJ*, 206, 218
- Gaia Collaboration, Babusiaux C. et al., 2018, *A&A*, 616, A10
- Gordon P., 1968, *Principles of Phase Diagrams in Materials Systems*, New York: McGraw-Hill
- Horowitz C. J., Schneider A. S., Berry D. K., 2010, *Phys. Rev. Lett.*, 104, 231101
- Ichimaru S., 1993, *Rev. Mod. Phys.*, 65, 255
- Jermyn A. S., Schwab J., Bauer E., Timmes F. X., Potekhin A. Y., 2021, *ApJ*, 913, 72
- Kozhberov A. A., Baiko D. A., *Physics of Plasmas*, 2015, 22, 092903
- Landau L. D., Lifshitz E. M., 1980, *Statistical Physics. Part I. Course of theoretical physics*, Oxford: Pergamon Press
- Lau R. et al., 2018, *ApJ*, 859, 62
- Medin Z., Cumming A., 2010, *Phys. Rev. E*, 81, 036107
- Ogata S., Iyetomi H., Ichimaru S., Van Horn H. M., 1993, *Phys. Rev. E*, 48, 1344
- Ott T., Baiko D. A., Kählert H., Bonitz M., 2013, *Phys. Rev. E*, 87, 043102
- Piersanti L., Tornambé A., Yungelson L. R., 2014, *MNRAS*, 445, 3239
- Potekhin A. Y., Chabrier G., 2000, *Phys. Rev. E*, 62, 8554
- Potekhin A. Y., Chabrier G., 2013, *A&A*, 550, A43
- Potekhin A. Y., Chabrier G., Chugunov A. I., DeWitt H. E., Rogers F. J., 2009, *Phys. Rev. E*, 80, 047401
- Roggero A., Reddy S., 2016, *Phys. Rev. C*, 94, 015803
- Segretain L., Chabrier G., 1993, *A&A*, 271, L13
- Shchepochin N. N., Chugunov A. I., 2019, *MNRAS*, 490, 3454
- Tremblay P.-E. et al., 2019, *Nature*, 565, 202
- Yakovlev D. G., Shalybkov D. A., 1989, *Sov. Sci. Rev., Ser. E: Astrophys. Space Phys.*, 7, 311
- Yakovlev D. G., Urpin V. A., 1980, *Sov. Astron.*, 24, 303